Origin of Enhanced Thermal Atomic Layer Etching of Amorphous HfO$_2$

Rita Mullins[1]; José Julio Gutiérrez Moreno[2] and Michael Nolan [1,a)]

[1]Tyndall National Institute, University College Cork, Cork T12 R5CP, Ireland.
[2]Barcelona Supercomputing Center (BSC), C/Jordi Girona 31, 08034 Barcelona, Spain

[a)] Electronic mail: michael.nolan@tyndall.ie

Abstract

HfO$_2$ is a high-k material that is used in semiconductor devices. Atomic-level control of material processing is required for the fabrication of thin films of high-k materials at nanoscale device sizes. Thermal atomic layer etching (ALE) of metal oxides, in which up to one monolayer of material can be removed, can be achieved by sequential self-limiting (SL) fluorination and ligand-exchange reactions at elevated temperatures. First-principles based atomic-level simulations using density functional theory (DFT) can give deep insights into the precursor chemistry and the reactions that drive the etch of metal oxides. A previous study examined the hydrogen fluoride (HF) pulse in the first step in the thermal ALE process of crystalline HfO$_2$ and ZrO$_2$. This study examines the HF pulse on amorphous HfO$_2$ using first-principles simulations. The Natarajan-Elliott analysis, a thermodynamic methodology is used to compare reaction models representing the self-limiting and spontaneous etch processes taking place during an ALE pulse. For the HF pulse on amorphous HfO$_2$, we found that thermodynamic barriers impeding spontaneous etching are present at ALE relevant temperatures. HF adsorption calculations on the amorphous oxide surface is studied to understand the mechanistic details of the HF pulse. A HF molecule adsorbs dissociatively by forming Hf-F and O-H bonds. HF coverages ranging from 1.1 ± 0.3 to 18.0 ± 0.3 HF/nm^2 are investigated and a mixture of molecularly and dissociatively adsorbed HF molecules is present at higher coverages. A theoretical etch rate of -0.82 ± 0.02 Å/cycle for amorphous HfO$_2$ was calculated using a maximum coverage

of 9.0 ± 0.3 Hf-F/nm^2. This theoretical etch rate is greater than the theoretical etch rate for crystalline HfO$_2$ that we previously calculated at -0.61 $\pm$ 0.02 Å/cycle. Undercoordinated atoms and void regions in amorphous HfO$_2$ allows for more binding sites during fluorination whereas crystalline HfO$_2$ has a limited number of adsorption sites.

I. INTRODUCTION

Atomic layer processing has become increasingly important due to the continued downscaling of semiconductor devices, which necessitates deposition of thinner materials films in complex structures. The control of film etch offered by thermal atomic layer etching (ALE) is necessary for state-of-the-art semiconductor devices.[1] Thermal ALE is a technique that removes thin layers of material using sequential, self-limiting surface reactions and can be viewed as the reverse of atomic layer deposition (ALD).[2] Thermal ALE is based on surface modification and volatilization reactions, where the modification step alters the surface layer into a non-volatile later followed by the release of volatile etch products from the surface layer in the second reaction.[2] For metal oxides, thermal ALE has been performed using fluorination and ligand exchange reactions as shown in Figure 1.[3] Fluorination converts the surface of the metal oxide to a surface fluoride layer and ligand exchange can volatilize the metal fluoride layer to produce stable etch products. Thermal ALE relies on temperature and thermochemically favourable reactions to remove surface species[4] and etches at the same rate in all directions.[5] Many technologically important metal oxides have been etched using thermal ALE including HfO$_2$,[6–9] ZrO$_2$,[6,9] SiO$_2$,[10] Al$_2$O$_3$,[9,11–17] TiO$_2$,[18] VO$_2$,[19] WO$_3$,[20] ZnO,[21] Ga$_2$O$_3$,[22] as well as metal nitrides such as

Si$_3$N$_4$,[23] AlN,[24] TiN,[25,26] and GaN.[27,28] Thermal ALE of amorphous Al$_2$O$_3$ has also been reported using NbF$_5$ to replace HF as the fluorination agent and CCl$_4$ for the halide-exchange reaction.[29] As well as fluorination and ligand-exchange, thermal ALE can also be performed by other processes such as conversion,[21] oxidation[25] oxidation/chlorination[30] and chlorine-fluorine ligand exchange.[31] Advantages of ALE include high uniformity, the ability to etch high-aspect-ratio features, selectivity, and smoothing.[32]
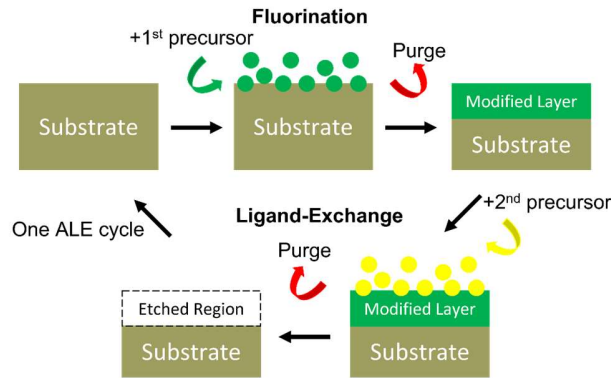

Figure 1. Schematic model of the thermal ALE process.

Semiconductor devices have features at the nanometer scale due to Moore's Law scaling. SiO$_2$ gate dielectrics are so thin that electron tunnelling through the dielectric layer, which leads to high leakage currents, is impossible to avoid.[33,34] HfO$_2$ is a high-k material with a dielectric constant of 22; it allows a high drive current to be maintained, while minimized leakage current meaning that a low equivalent oxide thickness can be used.[35] HfO$_2$ is thermodynamically stable when interfaced with silicon in semiconductor devices.[36,37] Amorphous HfO$_2$ has a dielectric constant of ~ 16 to 19.[38]

In terms of mechanisms, thermal ALE processes generally use HF for the fluorination step[25] for metal oxides as it is a useful nucleophilic fluorination reactant[19] in

which the fluoride anion serves as the active reaction species. For the ligand-exchange step examples of metal precursors used are $Sn(acac)_2$,[6] $Al(CH_3)_3$,[6,39] $Al(CH_3)_2Cl$,[6] $SiCl_4$,[6] BCl_3,[31] $TiCl_4$[8] and WF_6[40]. The surface fluorination step in thermal ALE using HF is the focus of our work and the focus of this paper.

Experimental studies have shown that crystalline films have lower etch rates than amorphous films for thermal ALE of metal oxides HfO_2, ZrO_2, $HfZrO_4$ at 250 °C and Al_2O_3 at 300 °C.[41,42] Using HF as the fluorinating agent and $TiCl_4$ as the ligand-exchange agent, the etch rate for amorphous HfO_2 was 18 times higher than the etch rate for crystalline HfO_2.[41] Using the same reagents, the etch rate for amorphous ZrO_2 was 2.3 times higher than the etch rate for crystalline ZrO_2.[41] Similarly using HF and dimethyl aluminium chloride (DMAC, $Al(CH_3)_2Cl$) the etch rate on amorphous HfO_2 was 8.5 times higher than the etch rate on crystalline HfO_2, whereas for ZrO_2 the amorphous etch rate was 1.4 times higher than the crystalline etch rate.[41] This shows for HfO_2 that the etch rates is strongly dependent on whether a crystalline or amorphous film is etched.[41] Amorphous materials have a lower density than their crystalline form, which may facilitate the fluorination that leads to an expansion of the metal oxide.[41] In wet HF etching, crystalline HfO_2 is also etched more slowly than amorphous HfO_2.[43] The differences in etch rates show potential for selective ALE where two different materials have different etch rates under the same conditions.[41]

Given that it is difficult to investigate thermal ALE reactions directly using experimental techniques, first-principles based atomic-level simulations using density functional theory (DFT) can give deep insights into the precursor chemistry and the reactions that drive the etch of metal oxides. Our previous study examined the difference

4

in thermal ALE for the fluorination step for crystalline HfO_2 and ZrO_2 using HF.[44] In the present paper, the HF pulse in the first step in thermal ALE of amorphous HfO_2 is examined in detail with first-principles DFT calculations of the fluorination mechanism. HF molecules adsorb at the surfaces of metal oxides by forming metal-F bonds and they may remain intact or dissociate.[45] If HF dissociates it may form Hf-F and O-H bonds, and release water, similar to previous studies on etch modelling for crystalline HfO_2, ZrO_2 and Al_2O_3.[44,45] The amount etched (etch rate) is determined by how much of the oxide surface is fluorinated; a larger fluoride film thickness after fluorination can lead to more fluoride removed during the ligand-exchange step and high etch rates.[41]

The Natarajan-Elliott analysis[44] (N-E) is used to predict the conditions at which a self-limiting (SL) or spontaneous etching (SE) reaction becomes thermodynamically favourable and can therefore be used to direct experimental studies of thermal ALE. Self-limiting reactions are a necessary part of thermal ALE and allow the degree of etching to be well controlled and defined. In this study, it is found that SL reactions are more favourable than the competing SE reaction for the HF pulse on amorphous HfO_2 at 0 and 520 K; the latter corresponds to the temperature used in experimental studies of thermal ALE for HfO_2 using HF as the fluorination agent[46]. The temperatures above which spontaneous etching is favoured range from 718 to 1302 K at typical thermal ALE reactant pressures, depending on the degree of fluorination; these are significantly higher than on crystalline HfO_2. Introducing HF molecules to the amorphous HfO_2 surface results in dissociative HF adsorption. The maximum coverage of Hf-F bonds on the surface is used to calculate a theoretical etch rate. The spontaneous formation of water and hydrogen peroxide is also discussed. Combining the thermodynamic and mechanistic investigation

5

using first-principles simulation demonstrates the origin of the large difference in etch rates for crystalline and amorphous HfO_2 allowing the design of novel ALE processes for other technologically relevant materials.

II. Computational Methods

All calculations reported in this paper were carried out using spin-polarized density functional theory implemented in VASP[47] 5.4. The Perdew-Burke-Ernzerhof (PBE) generalized gradient approximation (GGA) to exchange-correlation (XC) functional is used.[48] The convergence criteria for total energies and the forces for ionic relaxation are 1 x 10^4 eV and 2 x 10^{-2} eV/Å respectively. The Methfessel-Paxton first order smearing method is used with a broadening of 0.1 eV for the electronic relaxations. The core-valance electron interactions are represented by projector-augmented wave (PAW) potentials,[49] and the following valence electron configurations are used: Hf: $6s^2 5d^2$, O: $2s^2 2p^4$, F: $2s^2 2p^5$, and H: $1s^1$. The valence electrons are described with a periodic plane-wave basis set using a kinetic energy cutoff of 400 eV.

The Gibbs free energy, ΔG, at a temperature, T, is computed as follows:

$$\Delta G = \Delta H - T\Delta S + RTln(Q) \tag{1}$$

$$\Delta H = \Delta E + \Delta ZPE + \Delta W(T) \tag{2}$$

$$\Delta E = \sum_p \mu E_p - \sum_r \mu E_r \tag{3}$$

$$Q = \prod p_{products}^{\mu} / \prod p_{reactants}^{\mu} \tag{4}$$

The ΔH and ΔS terms in Eq. (1) are the changes in reaction enthalpy and reaction entropy respectively, with term $RT\ln(Q)$ included since the partial pressures of the reactants and products are variable in the reaction chamber. In Eq. (2), ΔH contains the electronic reaction energy at 0 K ΔE, zero-point energy change ΔZPE and a temperature-dependent enthalpy change ΔW(T). The stoichiometric coefficient of the corresponding species is μ and the reactant and product species are r and p respectively in Eq. (3). A reactant pressure of 0.2 Torr and a product pressure of 0.01 Torr are used for the free energy calculations. Of course, it is not possible to control the product pressure in an etch reactor. It is however, lower than the reactant pressure, so a value of 0.01 Torr for our calculations is consistent with this and previous work of DFT investigation in thermal etching of TiN.[50]

A.   Bulk and Slab Models

Bulk amorphous HfO_2 (henceforth $aHfO_2$) was prepared using classical molecular dynamics (MD) simulations with the LAMMPS package.[51] Atomic pair interactions were adopted from the Morse type potential developed by Broglia et al.[52] This potential is accurate for the simulation of glasses at high temperature and pressure and has been previously used for the study of $aHfO_2$.[52] The Nosé-Hoover thermostat in its isothermal-isobaric form (NPT) was used to set the constant pressure at 1 atm and the temperatures during the simulation. The integration time step was set to 0.1 fs. The amorphous structure was produced using the melt-quenching method. Initially, a total of 216 atoms with a stoichiometric HfO_2 composition (72 Hf and 144 O atoms) are randomly placed in a periodic cubic box. After an initial equilibration, the system is warmed up to 4000 K at a rate of 10 K/ps. The temperature was set well above the experimental melting point and

equilibrated for 2 ns to assure the initially random distribution of the atomic species in our model. The melted structure is then quenched to 300 K in consecutive steps of 10 K/ps (i.e. every 10^4 time-steps) and finally equilibrated for 1 ns at room conditions. The quenching rate was chosen to be quick enough to produce an amorphous structure at equilibrium; a pair distribution function is shown in Section 1 of the supplementary material. This procedure leads to an equilibrated cubic box with side dimensions of 13.72 Å. The density of the resulting simulation box is 9.62 g/cm^3, which is in good agreement with other aHfO$_2$ models generated by MD.[53–55] The surface model is cleaved from the bulk at a plane parallel to one of the box sides, where a large vacuum layer is introduced. To moderate the likely abundance of uncoordinated species at the surface formed from a random cleavage of the amorphous bulk, a rapid melt-quenching was run for the slab model keeping constant volume and temperature (NVT ensemble). The surface model was warmed to 4000 K at 20 K/ps rate, relaxed for 50 ps, quenched to 300 K at 10 K/ps rate, and finally equilibrated for 1 ns. The slab model is then relaxed using DFT.

The aHfO$_2$ bulk was relaxed by simultaneous relaxation of the ionic positions, cell volume and cell with an energy cutoff of 550 eV and a Monkhorst-Pack k-point sampling mesh of (1 x 1 x 1). The bulk aHfO$_2$ has 72 Hf and 144 O atoms and the optimized lattice constants are a = 13.729 Å, b = 13.871 Å and c = 13.796 Å and angles alpha = 90.74°, beta = 89.14° and gamma = 89.81°. The density of our bulk aHfO$_2$ model is 9.62 g/cm^3 which is smaller than the crystalline HfO$_2$ (monoclinic, cHfO$_2$) density from our previous study which was 10.01 g/cm^3.[44] The surface slab of aHfO$_2$ with 16 Å of vacuum separating the slabs is used for the surface models with a stoichiometry of Hf$_{72}$O$_{144}$ per supercell. A k-point sampling mesh of (2 x 2 x 1) is used for geometry optimization.

For the N-E analysis, the self-limiting reaction product state models are obtained by replacing every oxygen removed from the surface of the slab model with two fluorine atoms, this ratio is shown as 1O/2F.[44] Three self-limiting product state models: 8O/16F, 10O/20F and 16O/32F are examined. Enthalpy H and entropy S are computed using the Phonopy[56] code for only the top layers of fluorinated Hf atoms for the surface calculations For the gas phase molecules, H and S were calculated from the freeh program in the Turbomole[57,58] suite at 1 atm pressure using the PBE exchange-correlation functional[48] and a polarized triple basis set (def-TZVPP)[59,60] and default medium grid. The reactant molecules and gas-phase byproducts calculations are performed in VASP with a large periodic box of dimensions 15.0 Å x 16.0 Å x 15.5 Å and 400 eV plane-wave energy cutoff.

Experimental studies have shown that the chemical composition of $aHfO_2$ is essentially stoichiometric.[61] Theoretical studies of $aHfO_2$ reported that the coordination numbers for the Hf atoms were five, six, seven and eight with a preference for six and seven. For oxygen two, three and four coordination are found, with a preference for three and four coordination.[53] The distribution of the coordination numbers for the Hf and O atoms of the bulk $aHfO_2$ model used in this study is shown in Figure 2. To determine the coordination number, a cutoff radius of 2.50 Å derived from the behaviour of Hf-O bonds is used.[62] Three-coordinated O atoms and six-coordinated/seven-coordinated Hf atoms dominate the bulk $aHfO_2$ model which agrees with previous classical[63] and ab initio[64,65] molecular dynamic studies. Compared to the monoclinic phase, the coordination number for the Hf atoms can be seven or eightfold, and the O atoms can be either three or fourfold coordinated.[61]
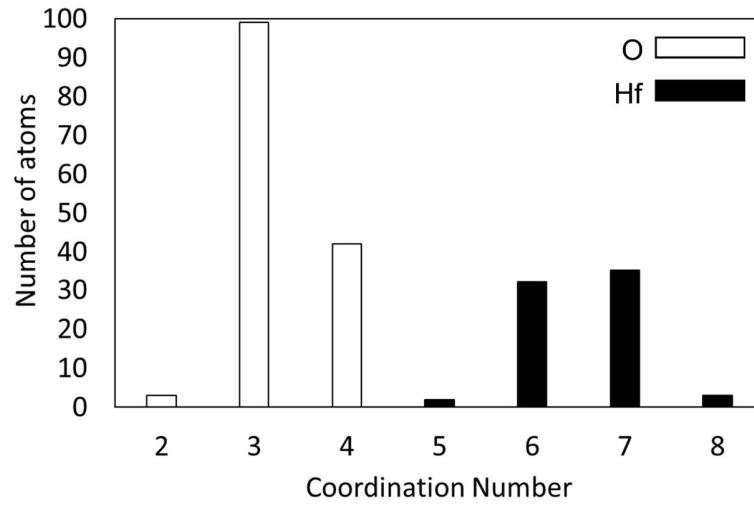
Figure 2. Distribution of coordination numbers for the bulk $aHfO_2$ model used in this study that was prepared using classical molecular dynamics.

III. RESULTS AND DISCUSSION

A. *Self-Limiting vs Spontaneous Etch*

To predict if the HF pulse will promote spontaneous etch (SE) or a self-limiting (SL) reaction on $aHfO_2$, the energetics and thermodynamics at given conditions are compared. Table *I* shows two possible SE and two possible SL reactions for the HF pulse on $aHfO_2$ as well as the reaction (free) energies at 0 K and at a typical thermal ALE temperature of 520 K and the computed minimum barrier to spontaneous etching. A negative minimum barrier would indicate that spontaneous etching is thermodynamically favourable and is prevented only by potential kinetic barriers.

Table I. Reaction energies at 0 K (ΔE) and free energies at 520 K (ΔG) from the model SE and SL reactions after the HF pulse on aHfO$_2$. For this table, the product state is 8O/16F and the numbers in parenthesis are the minimum barriers to continuous etching.

	Reactions	ΔE (eV/M)	ΔG (eV/M)
SE1	$1HfO_{2(b)} + 4HF_{(g)} \rightarrow 1HfF_{4(g)} + 2H_2O_{(g)}$	-1.44	-1.15
SL1	$1HfO_{2(surface)} + 4HF_{(g)} \rightarrow 1HfF_{4(surface)} + 2H_2O_{(g)}$	-4.07 (2.63)	-1.87 (0.72)
SE2	$1HfO_{2(b)} + 2HF_{(g)} \rightarrow 1HfOF_{2(g)} + 1H_2O_{(g)}$	3.35	2.58
SL2	$1HfO_{2(surface)} + 2HF_{(g)} \rightarrow 1HfOF_{2(surface)} + 1H_2O_{(g)}$	-2.04 (5.39)	-0.94 (3.52)

The SE1 and SE2 reactions convert the bulk aHfO$_2$ into a volatile metal fluoride or metal oxyfluoride, respectively, and water. In reaction SE1, four HF molecules are required to etch one unit of bulk HfO$_2$ forming HfF$_4$ and water. In reaction SE2, two HF molecules are needed to etch one unit of HfO$_2$ to form HfOF$_2$ and H$_2$O. In both SE reactions, the surface of the material before and after each precursor pulse is identical and therefore their contributions are not required in these models.

The SL1 and SL2 reactions involve the conversion of the outermost surface layer of aHfO$_2$ into the nonvolatile metal fluoride and nonvolatile metal oxyfluoride respectively with the release of water molecules. The SL product state of the surface is 8O/16F where eight oxygen were removed and replaced by sixteen fluorine. For both SL reactions, the surfaces are not identical before and after the pulse and their contributions have to be included. A negative free energy means that the corresponding reaction is exergonic (favourable), while a positive free energy means that the corresponding reaction is endergonic (unfavourable). At 0 and 520 K, the SE1 reaction is favourable whereas the

SE2 reaction is unfavorable. Table I shows that the barrier to spontaneous etch is positive for all the SE and SL reactions at 0 K, indicating that the self-limiting reaction is most favourable energetically and at 520 K this barrier to spontaneous etching, although reduced, remains positive. Therefore, up to 520 K, the reactions with HF in the first step will be preferentially self-limiting on aHfO$_2$, similar to crystalline HfO$_2$.

Only the SE1 reaction is considered for further analysis, as the SE2 reaction is unfavorable at 0 and 520 K and the SL2 reaction is less favorable than the SL1 reaction at 0 and 520 K. In addition, the high barrier to etch for the SL2 and SE2 reactions suggests that spontaneous formation of the metal oxyfluoride is not likely at ALE-relevant temperatures around 520 K. The reaction free energy profiles (FEPs) of the SE1 and SL1 reactions are shown in Figure *3* and at a given temperature and reactant pressure these show whether spontaneous etching or self-limited conversion of aHfO$_2$ into a nonvolatile metal fluoride layer are preferred. A reactant pressure of 0.2 Torr and a product pressure of 0.01 Torr are used and the temperature range is 0−1000 K.
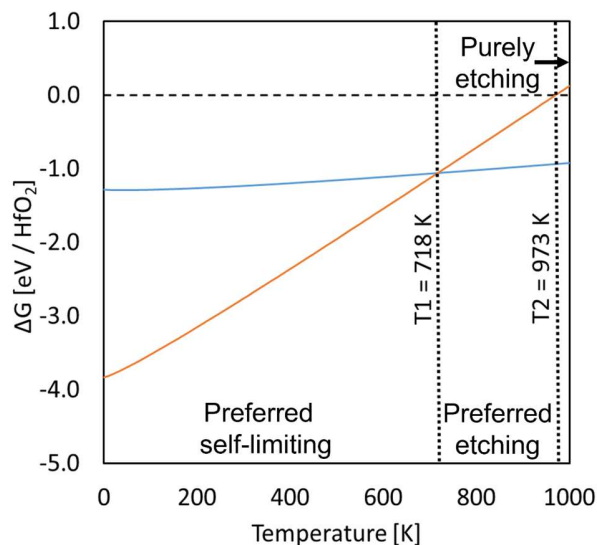
Figure 3. Free energy profile for the SE1 (blue) and SL1 (orange) reactions of aHfO$_2$ from 0 to 1000 K at the pressures given in the text. T1 is where the SL and SE reactions cross over for the 8O/16F model, and T2 is where spontaneous etching is preferred.

In Figure *3* the self-limiting reaction is preferred up to 717 K, at 718 K the minimum barrier to etch is zero with SE1 and SL1 being isoenergetic and at temperatures higher than 718 K spontaneous etching becomes more favourable. At 973 K, the self-limiting reaction becomes unfavourable while spontaneous etching remains favourable. Surface hafnium atoms are easier to remove in the ligand-exchange step when more oxygen atoms are removed due to the reduced hafnium-oxygen bonds interaction. The surface of aHfO$_2$ has 19 oxygen atoms in the supercell that could react with the HF molecules, therefore we study the FEPs for two other SL product models, 10O/20F (SL2) and 16O/32F (SL3) as shown in Table *II* and Figure *4* to compare their thermodynamic stability with the 8O/16F model. For the 10O/20F model, 10 of the surface oxygen are removed and 20 fluorine are added to replace them. For the 16O/32F, 16 oxygen are removed and 32 fluorine are added to replace them. All three SL product states are more favourable than the SE reaction at 0

13

and 520 K with positive minimum barriers as shown in Table *II*. Experimental work showed that the HF reaction is self-limiting on amorphous HfO_2 at 250 °C (523 K).[41] Figure *4* shows that the self-limiting product state models are more favourable than the spontaneous etch reaction at 523 K with the 16O/32F (SL3) being favourable up to 1302 K.

Table II. Reaction (free) energies and minimum barriers at 0 and 520 K for the model self-limiting for 8O/16F, 10O/20F and 16O/32F SL product states.

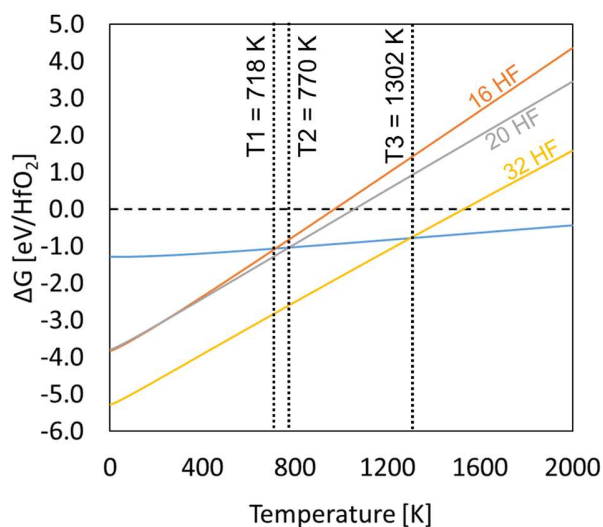|	SL Product State	ΔE (0 K) (eV/M)	ΔG (520 K) (eV/M)
SE1	HfF_4	-1.44	-1.15
SL1	8O/16F	-4.07 (2.63)	-1.87 (0.72)
SL2	10O/20F	-4.02 (2.58)	-1.97 (0.82)
SL3	16O/32F	-5.51 (4.07)	-3.48 (2.33)

Figure 4. Free energy profiles of the spontaneous etching and self-limiting reactions for aHfO$_2$. T1, T2 and T3 are the temperatures where the self-limiting and spontaneous etch reactions cross over for 8O/16F, 10O/20F and 16O/32F models respectively.

B. *Adsorption of one HF to the bare amorphous HfO$_2$ surface*

One HF molecule was adsorbed at the bare surface of aHfO$_2$ on different binding sites (labelled A, B and C) that were chosen at random as typical binding sites. At each binding site the HF molecule spontaneously dissociated to form Hf−F and O−H bonds as shown in Figure 5. Similar to the crystalline HfO$_2$ and ZrO$_2$[44], HF dissociation proceeds after a stable metal-fluorine bond is formed. The Hf−F and O−H bond lengths are shown for each binding site in Figure 5. The computed adsorption energies for the dissociative adsorption of one HF molecule on the bare surface of aHfO$_2$ are −2.17, −2.92, and −2.00 eV at sites A, B, and C, respectively. These adsorption energies are more negative than on cHfO$_2$, most likely as a result of the surface disorder and range of coordination numbers of the surface atoms. This indicates that the fluorination steps in thermal self-limiting etch of

15

aHfO$_2$ would proceed faster than on cHfO$_2$. The surface O atoms are 1-fold, 2-fold or 3-fold coordinated by surface Hf atoms with the 3-fold being dominant in the model used in this study. The surface Hf atoms are 5-fold, 6-fold or 7-fold coordinated by surface O atoms with the 6-fold being dominant in the model used in this study. The lower coordination numbers in aHfO$_2$ promote the interaction with HF and metal fluorination.
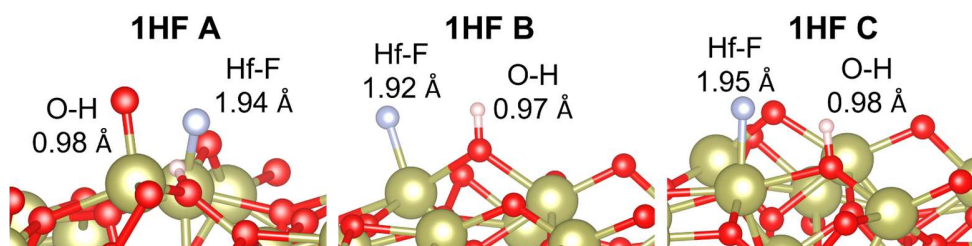

Figure 5. Relaxed adsorption structures for one HF molecule interacting with the bare surface of aHfO$_2$. The colour coding is brown = Hf, red = O, white = H and blue = F.

C. Stability of Higher HF Coverages

Similar to our previous study on crystalline HfO$_2$ and ZrO$_2$, higher HF coverages were examined by introducing up to 34 randomly oriented HF molecules per supercell approximately 3 Å from the bare surface of aHfO$_2$. This was studied to see if higher HF coverages would result in complete dissociation or a mixture of molecular and dissociative adsorption of the HF molecules. There are 18 topmost hafnium atoms on the surface of the supercell that may form Hf−F bonds and 19 surface oxygen atoms that can form O−H bonds or as seen in some cases H$_2$O and H$_2$O$_2$. For HF coverages using 2, 3, 4, 5, and 8 molecules per supercell three different configurations (labelled A, B and C) were used, for the 16 HF coverages two configurations (A and B) were used and one configuration for HF coverages of 28, 30, 32 and 34 molecules per supercell. Some configurations from HF coverages of 2, 3, 4 and 5 HF resulted in spontaneous complete dissociation of the adsorbed

HF molecules as shown in Figure 6. There was a mixture of molecular and dissociative adsorption of the HF molecules in all other HF adsorption configurations (see Section 2 of the supplementary material for their geometries). The molecular adsorbed HF molecules are likely to remain bonded to the surface in the next ALE step as they form strong bonds (Hf-F 6.7 eV)[66] and would likely dissociate when the kinetic barriers are reduced in the reactor during the ALE process. Similar to our previous study[44] on crystalline HfO_2, the HF molecules that did not dissociate in the relaxed geometries form hydrogen bonds with the remaining HF molecules and dissociated F atoms and at higher HF coverages a more extensive hydrogen-bonded network is expected.
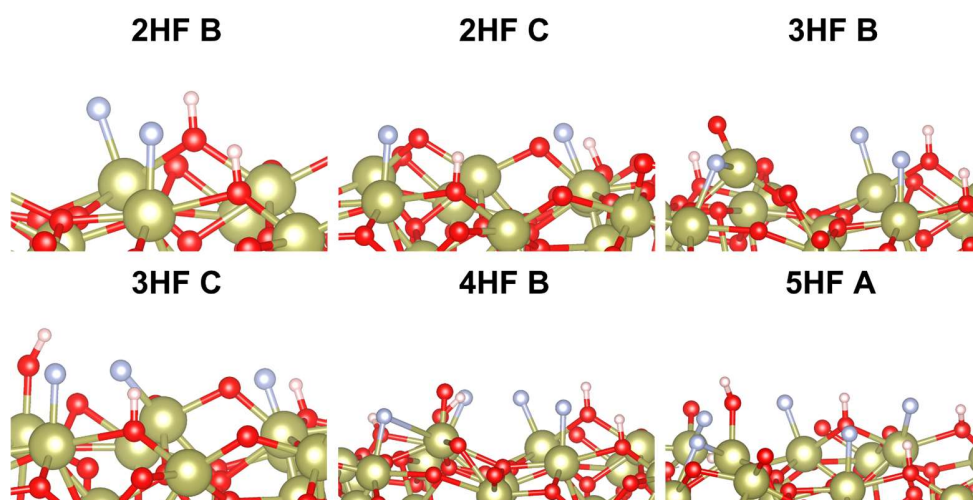

Figure 6. Relaxed geometries for HF coverages 2HF B, 2HF C, 3HF B, 3HF C, 4HF B and 5HF A of amorphous HfO_2 where complete dissociation of HF occurred spontaneously. Colour coding is the same as in Figure 5.

The binding energies per HF and per unit surface area of the material were computed as shown in Table III. As the number of Hf-F bonds increases on the bare $aHfO_2$ surface with higher HF coverages, the binding energy per surface area becomes more

favourable as shown in Table III and Figure 7(c) with Hf-F coverage from 1.1 ± 0.3 to 9.0 ± 0.3 HF/nm^2 with surface binding energies -5.3 to -20.0 eV/nm^2 (see Section 3 of the supplementary material for the error bar explanation).

Table III. Adsorbate coverages and binding energies for the HF coverages on aHfO$_2$.

Geometry	Adsorbed HF (nm^{-2})	Hf-F (nm^{-2})	Dissociated HF (nm^{-2})	Ebind (eV/HF)	Ebind (eV/nm^2)
2HF A	1.1	0.5	0.5	-1.3	-1.4
2HF B	1.1	1.1	1.1	-2.2	-2.4
2HF C	1.1	1.1	1.1	-5.0	-5.3
3HF A	1.6	1.1	1.1	-1.7	-2.7
3HF B	1.6	1.6	1.6	-1.7	-2.8
3HF C	1.6	1.6	1.6	-2.3	-3.6
4HFA	2.1	1.6	1.6	-3.4	-7.2
4HFB	2.1	2.1	2.1	-1.8	-3.8
4HFC	2.1	1.6	1.6	-1.9	-3.9
5HFA	2.7	2.7	2.7	-3.4	-8.9
5HFB	2.7	2.7	2.7	-3.1	-8.1
5HFC	2.7	2.1	2.1	-1.7	-4.4
8HFA	4.2	3.7	3.2	-1.6	-6.6
8HFB	4.2	3.7	3.2	-1.6	-6.7
8HFC	4.2	3.2	2.7	-2.2	-9.4
16HFA	8.5	6.4	5.3	-1.7	-14.6
16HFB	8.5	3.7	3.7	-1.2	-9.9
28HF	14.8	6.9	6.4	-1.2	-17.7
30HF	15.9	7.4	5.3	-1.1	-17.9

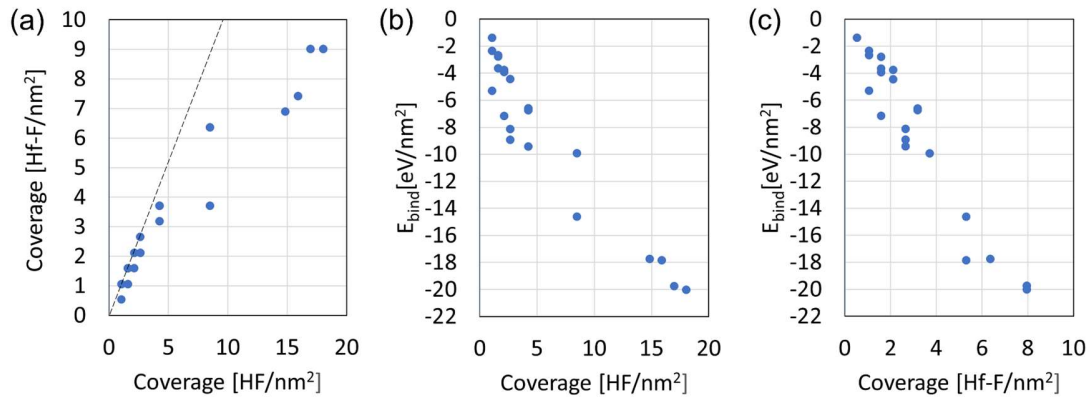|					
32HF	16.7	9.0	8.0	-1.2	-19.8
34HF	18.0	9.0	8.0	-1.1	-20.0

Figure 7 (a) Scatter plot for Hf-F coverage versus total HF coverage for the surface coverage values in Table III. Plots (b) and (c) show the change in binding energy per square nanometer with an increase in HF and Hf-F coverage, respectively.

Hf-F coverage versus adsorbed HF coverage is shown in plot (a) in Figure 7 with the HF coverages that resulted in complete dissociation lying along the correlation line. This corresponds to coverages of 1.1, 1.6, 2.1 and 2.7 HF/nm^2. The remaining data points are HF coverages that correspond to geometries where partially dissociated HF and molecular adsorbed HF molecules are present and therefore lie below the correlation line. The Hf-F coverage starts to plateau at higher HF coverages suggesting a maximum coverage of 9.0 ± 0.3 Hf-F/nm^2. Also note that the number of Hf-F/nm^2 is the same for HF coverages 32 and 34 HF. It is also shown that a saturation in the binding energy is not reached at high HF coverages and Hf-F coverages respectively as shown in plots (b) and

(c) in Figure 7. We use the highest adsorbed HF coverage of 34 HF with Hf-F coverage of 9.0 ± 0.3 Hf-F/nm^2 as the maximum coverage for the aHfO$_2$ etch rate prediction.

D. *Spontaneous Formation of H$_2$O and H$_2$O$_2$*

H$_2$O spontaneously formed in some of the relaxed geometries such as 5HF C, 8HF C and 16 HF A as shown in Figure 8. The dissociation of at least two HF molecules provides the hydrogen atoms required to form H$_2$O as a reaction product which removes oxygen from aHfO$_2$ during ALE. The H-O-H bond angles were 103.5°, 105.1° and 108.0° for 5HF C, 8HF C and 16 HF A as shown in Figure 8. The energy to remove H$_2$O (energy of desorption) from the fluorinated surfaces of 5HF C, 8HF C and 16 HF A, as typical examples where water was formed, was calculated using Eq. (5).

$$E_{des} = (E_{HfO_{2(surf)}/HF_{(ads)}} + E_{H_2O_{(g)}}) - (E_{HfO_{2(surf)}/HF_{(ads)}/H_2O_{(ads)}}) \qquad (5)$$

The total energy of HF adsorbed on aHfO$_2$ with the spontaneous H$_2$O formed is represented by the term "$E_{HfO_{2(surf)}/HF_{(ads)}/H_2O_{(ads)}}$". H$_2$O was removed from the fluorinated surface and the resulting geometry was relaxed. The term "$E_{HfO_{2(surf)}/HF_{(ads)}}$" is the total energy of HF adsorbed on aHfO$_2$ after removing H$_2$O from the surface and "$E_{H_2O_{(g)}}$" is the energy of gas-phase H$_2$O molecule. The desorption energies of H$_2$O on geometries 5HF C, 8HF C and 16 HF A are 1.97, 1.47 and 1.67 eV respectively. With the high energy gain from HF adsorption at aHfO$_2$, we expect facile water desorption once it is formed.

5HF C   **8HF C**   **16HF A**
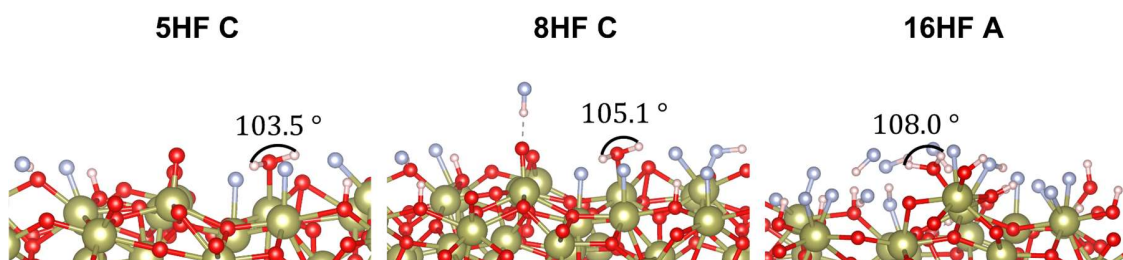
103.5 °   105.1 °   108.0 °

Figure 8. Relaxed geometries for HF coverages 5HF C, 8HF C and 16HF A where H_2O formed spontaneously. Colour coding is the same as in Figure 5.

The spontaneous formation of H_2O_2 was also observed at higher HF coverages such as 28HF as shown in Figure 9. Similar to H_2O, the dissociation of at least two HF molecules provides the hydrogen atoms required to form H_2O_2 as a reaction product which removes oxygen from aHfO$_2$. The H_2O_2 formed in Figure 9 had an O-O bond length of 1.47 Å, O-H bond lengths of 1.05 Å and 1.02 Å and H-O-O bond angles 100.3° and 104.5°. The energy to remove H_2O_2 (energy of desorption) from the fluorinated surface of 28HF was calculated using Eq. (5) where the "H_2O" terms were replaced with "H_2O_2". The desorption energy was calculated to be 0.47 eV which is low and can be achievable at process conditions to remove H_2O_2. Only the spontaneous formation of H_2O was observed in our previous study of HF coverages on crystalline HfO_2 and ZrO_2.[44]
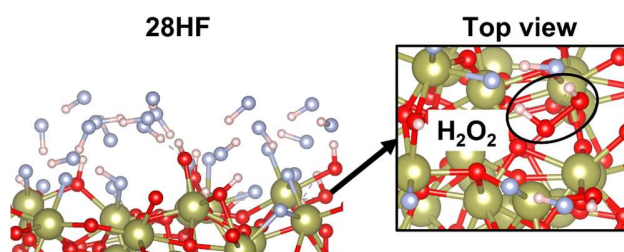

28HF   **Top view**

H_2O_2

Figure 9. Relaxed geometry for 28HF where H_2O_2 formed spontaneously. Colour coding is the same as in Figure 5.

E. Discussion

Comparing the spontaneous etch reaction to the self-limiting reaction for the 8O/16F SL product state model, at all temperatures less than 520 K using reactant and product pressures of 0.2 and 0.01 Torr respectively, the HF pulse on aHfO$_2$ is self-limiting in nature as the reaction energies for the self-limiting reaction were more favourable than the spontaneous etch reaction. From this, it is suggested that the first precursor pulse using HF will produce a stable and non-volatile layer of metal fluorides and H$_2$O or H$_2$O$_2$ as byproducts. The reaction energies for the SL product state models 8O/16F and 10O/20F were similar up to 400 K due to the small difference in the degree of fluorination between the models. The 16O/32F SL product state model reaction energies were more favourable than the 8O/16F and 10O/20F reactions up to 1302 K. Comparing to our previous study examining the fluorination step of crystalline HfO$_2$, the reaction energies for the 16O/32F product state model were less favourable than the partially fluorinated SL product state models.[44] The greater the degree of fluorination on aHfO$_2$, the more favourable the reaction energies are, showing aHfO$_2$ favours higher fluorine content SL product states than less fluorinated SL product states, which will promote the self-limiting surface modification step. The replacement of oxygen with fluorine during fluorination may be easier due to the lower density of amorphous materials compared to crystalline materials.[41]

HF coverages on aHfO$_2$ ranging from 1.1 ± 0.3 to 18.0 ± 0.3 HF/nm^2 resulted in complete dissociation or mixed dissociated and molecular HF adsorption. Water and hydrogen peroxide form spontaneously after relaxation and their computed desorption energies are low enough to be overcome at process conditions. A maximum coverage of 9.0 ± 0.3 Hf-F/nm^2 was found at higher HF coverages to be used to calculate a theoretical

etch rate. The surface area of the $aHfO_2$ supercell is 1.88 nm^2 with 18 Hf atoms that can form Hf-F bonds that correspond to a coverage of 9.5 ± 0.3 Hf/nm^2. Using the maximum coverage of Hf-F 9.0 ± 0.3 Hf-F/nm^2 there will be about 0.95 F atoms per surface Hf. Similar to the analysis done in previous theoretical etch rate calculations for crystalline Al_2O_3,[45] HfO_2 and ZrO_2,[44] the amount of Hf that can be etched is one-quarter of the Hf-F coverage which is 2.3 ± 0.1 Hf/ (nm^2 cycle) for $aHfO_2$. As the surface concentration of Hf atoms is 9.5 ± 0.3 Hf/nm^2, this etch rate corresponds to 0.2 monolayer/cycle. This corresponds to -78.8 ± 0.8 ng/ (cm^2 cycle) and using our DFT density of bulk $aHfO_2$ (9.62 g/cm^3), our theoretical etch rate for $aHfO_2$ is -0.82 ± 0.02 Å/cycle. Our theoretical etch rate for $cHfO_2$ is -0.61 ± 0.02 Å/cycle.[44] The theoretical etch rate for $aHfO_2$ is greater than the theoretical etch rate for $cHfO_2$ by 0.21 Å/cycle. Etch rates calculated from experiment can differ with temperature and the reactant used in the second pulse. It was found experimentally using HF as the fluorinating reagent and DMAC as the ligand-exchange reagent at 250 °C the etch rate was 0.68 Å/cycle for $aHfO_2$ and 0.08 Å/cycle for $cHfO_2$.[41] Using HF as the fluorinating reagent and $TiCl_4$ as the ligand-exchange reagent at 250 °C the etch rate was 0.36 Å/cycle for $aHfO_2$ and 0.02 Å/cycle for $cHfO_2$.[41] We therefore qualitatively show the enhanced etch rate for $aHfO_2$ compared to $cHfO_2$, and provide origins of this enhanced etching on $aHfO_2$.

Unlike experimental etch rates, theoretical etch rates do not take kinetic effects into account. Hence, the maximum etch rate to remove a monolayer (ML) of material from $aHfO_2$ is also calculated. For one ML removal, 18 Hf atoms are used which requires a Hf-F coverage of 38.2 ± 0.3 F/nm^2. An etch rate of -3.47 Å/cycle was computed for one ML removal using the same method for calculating the theoretical etch rate. If an experimental

etch rate was greater than -3.47 Å/cycle it would suggest that subsurface Hf atoms are being etched and the reaction is no longer self-limiting. The published etch rates for metal oxides[41] are much lower than this maximum etch rate further confirming that self-limiting etching is indeed observed.

The difference seen in thermal ALE etch rates of amorphous and crystalline HfO_2 may be due to higher density crystalline materials having bond lengths and configurations that are more uniform than for amorphous materials.[41] Amorphous materials may have void regions and undercoordinated atoms that allows for more binding sites during fluorination. HF adsorption studies for crystalline HfO_2 showed that every surface-bound F atom had a coordination number of one with surface Hf for Hf-F coverage of 7.0 ± 0.3 F/nm^2.[44] For amorphous HfO_2, the coordination number for surface-bound F atoms range from one to three, for a Hf-F coverage of 9.0 ± 0.3 F/nm^2. The greater the surface is fluorinated; the more material can be removed and a greater etch rate is obtained.

IV. SUMMARY AND CONCLUSIONS

In this paper, we present DFT calculations to understand the nature of the HF pulse on amorphous HfO_2 for thermal ALE. A thermodynamic analysis of the self-limiting and spontaneous etch reactions representing the fluorination on amorphous HfO_2 allowed us to predict whether the SE or SL reaction is favourable at a given temperature and a given pressure. At temperatures less than 520 K, the HF reaction is found to be in the preferred self-limiting state. This is a relatively inexpensive way to screen the reactant molecules for ALE of any given substrate. The adsorption of HF molecules on amorphous HfO_2 for HF coverages ranging from 1.1 ± 0.3 to 18.0 ± 0.3 HF/nm^2 along with analysis of H_2O and

H_2O_2 formation was studied. From this analysis, we predict a theoretical etch rate based on the maximum possible coverage of surface-bound HF for amorphous HfO_2 which was calculated to be -0.82 ± 0.02 Å/cycle. This computed etch rate for amorphous HfO_2 is greater than the etch rate computed for crystalline HfO_2 from our previous study. We can use the presented methodology for the first pulse on crystalline and amorphous metal oxides to examine other reagents such as SF_4 and XeF_2 with a similar analysis.

SUPPLEMENTAL MATERIAL

See supplementary material at [URL will be inserted by AIP Publishing] for the following (i) the pair distribution function of the amorphous HfO_2 bulk model used in this study, (ii) figures of the mixed molecular and dissociative adsorption of the HF molecules at the $aHfO_2$ surface and (iii) explanation of the ± 0.3 error bar.

ACKNOWLEDGMENTS

DATA AVAILABILITY

The data that support the findings of this study are openly available at

https://github.com/RitaMull/Thermal-ALE-aHfO2-using-HF

REFERENCES

[1] K.J. Kanarik, T. Lill, E.A. Hudson, S. Sriraman, S. Tan, J. Marks, V. Vahedi, and R.A. Gottscho, Journal of Vacuum Science & Technology A: Vacuum, Surfaces, and Films **33**, 020802 (2015).

[2] S.M. George, Accounts of Chemical Research **53**, 1151 (2020).

[3] S.M. George and Y. Lee, ACS Nano **10**, 4889 (2016).

[4] Y. Lee and S.M. George, ACS Nano **9**, 2061 (2015).

[5] A. Fischer, A. Routzahn, S.M. George, and T. Lill, Journal of Vacuum Science & Technology A **39**, 030801 (2021).

[6] Y. Lee, C. Huffman, and S.M. George, Chemistry of Materials **28**, 7657 (2016).

[7] Y. Lee, J.W. DuMont, and S.M. George, ECS Journal of Solid State Science and Technology **4**, N5013 (2015).

[8] Y. Lee and S.M. George, Journal of Vacuum Science & Technology A **36**, 061504 (2018).

[9] Y. Lee and S.M. George, Journal of Physical Chemistry C **123**, 18455 (2019).

[10] J.W. DuMont, A.E. Marquardt, A.M. Cano, and S.M. George, ACS Applied Materials and Interfaces **9**, 10296 (2017).

[11] Y. Lee, J.W. DuMont, and S.M. George, Chemistry of Materials **27**, 3648 (2015).

[12] Y. Lee and S.M. George, ACS Nano **9**, 2061 (2015).

[13] Y. Lee, J.W. DuMont, and S.M. George, Chemistry of Materials **28**, 2994 (2016).

[14] J. Hennessy, C.S. Moore, K. Balasubramanian, A.D. Jewell, K. France, and S. Nikzad, Journal of Vacuum Science & Technology A: Vacuum, Surfaces, and Films **35**, 041512 (2017).

[15] J.W. DuMont and S.M. George, The Journal of Chemical Physics **146**, 052819 (2017).

[16] A. Fischer, A. Routzahn, Y. Lee, T. Lill, and S.M. George, Journal of Vacuum Science & Technology A: Vacuum, Surfaces, and Films **38**, 022603 (2020).

[17] J. Hennessy, A.D. Jewell, J.P. Jones, G.M. Crouch, and S. Nikzad, ACS Applied Materials and Interfaces **13**, 4723 (2021).

[18] P.C. Lemaire and G.N. Parsons, Chemistry of Materials **29**, 6653 (2017).

[19] J.C. Gertsch, A.M. Cano, V.M. Bright, and S.M. George, Chemistry of Materials **31**, 3624 (2019).

[20] N.R. Johnson and S.M. George, ACS Applied Materials and Interfaces **9**, 34435 (2017).

[21] D.R. Zywotko and S.M. George, Chemistry of Materials **29**, 1183 (2017).

[22] Y. Lee, N.R. Johnson, and S.M. George, Chemistry of Materials **32**, 5937 (2020).

[23] A.I. Abdulagatov and S.M. George, Journal of Vacuum Science & Technology A **38**, 022607 (2020).

[24] N.R. Johnson, H. Sun, K. Sharma, and S.M. George, Journal of Vacuum Science & Technology A: Vacuum, Surfaces, and Films **34**, 050603 (2016).

[25] Y. Lee and S.M. George, Chemistry of Materials **29**, 8202 (2017).

[26] K. Shinoda, N. Miyoshi, H. Kobayashi, M. Izawa, K. Ishikawa, and M. Hori, Journal of Physics D: Applied Physics **52**, 475106 (2019).

[27] T. Ohba, W. Yang, S. Tan, K.J. Kanarik, and K. Nojiri, Japanese Journal of Applied Physics **56**, 06HB06 (2017).

[28] C. Kauppinen, S.A. Khan, J. Sundqvist, D.B. Suyatin, S. Suihkonen, E.I. Kauppinen, and M. Sopanen, Journal of Vacuum Science & Technology A: Vacuum, Surfaces, and Films **35**, 060603 (2017).

[29] V. Sharma, S.D. Elliott, T. Blomberg, S. Haukka, M.E. Givens, M. Tuominen, and M. Ritala, Chemistry of Materials **33**, 2883 (2021).

[30] S.K. Natarajan, M. Nolan, P. Theofanis, C. Mokhtarzadeh, and S.B. Clendenning, Cite This: ACS Appl. Mater. Interfaces **12**, 36680 (2020).

[31] P.C. Lemaire and G.N. Parsons, Chemistry of Materials **29**, 6653 (2017).

[32] K.J. Kanarik, S. Tan, and R.A. Gottscho, J. Phys. Chem. Lett **9**, 4814 (2018).

[33] G.D. Wilk, R.M. Wallace, and J.M. Anthony, Journal of Applied Physics **89**, 5243 (2001).

[34] P. Raghu, C. Yim, F. Shadman, and E. Shero, AIChE Journal **50**, 1881 (2004).

[35] P. Raghu, N. Rana, C. Yim, E. Shero, and F. Shadman, Journal of The Electrochemical Society - J ELECTROCHEM SOC **50**, 1881 (2003).

[36] D.M. Hausmann, E. Kim, J. Becker, and R.G. Gordon, Chemistry of Materials **14**, 4350 (2002).

[37] E. Cockayne, Journal of Applied Physics **103**, 084103 (2008).

[38] P.R. Chalker, M. Werner, S. Romani, R.J. Potter, K. Black, H.C. Aspinall, A.C. Jones, C.Z. Zhao, S. Taylor, and P.N. Heys, Applied Physics Letters **93**, 182911 (2008).

[39] R. Rahman, E.C. Mattson, J.P. Klesko, A. Dangerfield, S. Rivillon-Amy, D.C. Smith, D. Hausmann, and Y.J. Chabal, ACS Applied Materials & Interfaces **10**, 31784 (2018).

[40] W. Xie, P.C. Lemaire, and G.N. Parsons, ACS Applied Materials & Interfaces **10**, 9147 (2018).

[41] J.A. Murdzek and S.M. George, Journal of Vacuum Science & Technology A **38**, 022608 (2020).

[42] J.A. Murdzek, A. Rajashekhar, R.S. Makala, and S.M. George, Journal of Vacuum Science & Technology A **39**, 042602 (2021).

[43] J. Chen, W. Jong Yoo, and D.S.H. Chan, Journal of The Electrochemical Society **153**, G483 (2006).

[44] R. Mullins, S. Kondati Natarajan, S.D. Elliott, and M. Nolan, Chemistry of Materials **32**, 3414 (2020).

[45] S. Kondati Natarajan and S.D. Elliott, Chemistry of Materials **30**, 5912 (2018).

[46] C. Fang, Y. Cao, D. Wu, and A. Li, Progress in Natural Science: Materials International **28**, 667 (2018).

[47] G. Kresse and J. Furthmüller, Physical Review B **54**, 11169 (1996).

[48] J.P. Perdew, K. Burke, and M. Ernzerhof, Physical Review Letters **77**, 3865 (1996).

[49] G. Kresse and D. Joubert, Physical Review B **59**, 1758 (1999).

[50] V. Sharma, S. Kondati Natarajan, S.D. Elliott, T. Blomberg, S. Haukka, M.E. Givens, M. Tuominen, and M. Ritala, Advanced Materials Interfaces 2101085 (2021).

[51] S. Plimpton, Journal of Computational Physics **117**, 1 (1995).

[52] G. Broglia, G. Ori, L. Larcher, and M. Montorsi, Modelling and Simulation in Materials Science and Engineering **22**, 065006 (2014).

[53] D. Ceresoli and D. Vanderbilt, Physical Review B **74**, 125108 (2006).

[54] W. Shen, N. Kumari, G. Gibson, Y. Jeon, D. Henze, S. Silverthorn, C. Bash, and S. Kumar, Journal of Applied Physics **123**, 085113 (2018).

[55] J. Strand, M. Kaviani, V. v Afanas'ev, J.G. Lisoni, and A.L. Shluger, Nanotechnology **29**, 125703 (2018).

[56] A. Togo and I. Tanaka, Scripta Materialia **108**, 1 (2015).

[57] TURBOMOLE v6.2 2010, A Development of University of Karlsruhe and Forschungszentrum Karlsruhe GmbH, 1989-2007, TURBOMOLE GmbH, since 2007. Available from http://www.turbomole.com (Last Accessed 27 Nov, 2019).

[58] S.G. Balasubramani, G.P. Chen, S. Coriani, M. Diedenhofen, M.S. Frank, Y.J. Franzke, F. Furche, R. Grotjahn, M.E. Harding, C. Hättig, A. Hellweg, B. Helmich-Paris, C. Holzer, U. Huniar, M. Kaupp, A. Marefat Khah, S. Karbalaei Khani, T. Müller, F. Mack, B.D. Nguyen, S.M. Parker, E. Perlt, D. Rappoport, K. Reiter, S. Roy, M. Rückert, G. Schmitz, M. Sierka, E. Tapavicza, D.P. Tew, C. van Wüllen, V.K. Voora, F. Weigend, A. Wodyński, and J.M. Yu, Journal of Chemical Physics **152**, 184107 (2020).

[59] A. Schäfer, H. Horn, and R. Ahlrichs, The Journal of Chemical Physics **97**, 2571 (1992).

[60] A. Schäfer, C. Huber, and R. Ahlrichs, The Journal of Chemical Physics **100**, 5829 (1994).

[61] T. v. Perevalov, V.A. Gritsenko, S.B. Erenburg, A.M. Badalyan, H. Wong, and C.W. Kim, Journal of Applied Physics **101**, 053704 (2007).

[62] T.J. Chen and C.L. Kuo, Journal of Applied Physics **110**, 064105 (2011).

[63] Y. Wang, F. Zahid, J. Wang, and H. Guo, Physical Review B - Condensed Matter and Materials Physics **85**, 224110 (2012).

[64] W.L. Scopel, A.J.R. da Silva, and A. Fazzio, Physical Review B - Condensed Matter and Materials Physics **77**, 172101 (2008).

[65] G.H. Chen, Z.F. Hou, and X.G. Gong, Applied Physics Letters **95**, 102905 (2009).

[66] Y.R. Luo, Comprehensive Handbook of Chemical Bond Energies 1 (2007).